3

High Resolution X-Ray Spectroscopy with Compound Semiconductor Detectors and Digital Pulse Processing Systems

Leonardo Abbene and Gaetano Gerardi
Dipartimento di Fisica, Università di Palermo
Italy

1. Introduction

The advent of semiconductor detectors has revolutionized the broad field of X-ray spectroscopy. Semiconductor detectors, originally developed for particle physics, are now widely used for X-ray spectroscopy in a large variety of fields, as X-ray fluorescence analysis, X-ray astronomy and diagnostic medicine. The success of semiconductor detectors is due to several unique properties that are not available with other types of detectors: the excellent energy resolution, the high detection efficiency and the possibility of development of compact detection systems. Among the semiconductors, silicon (Si) detectors are the key detectors in the soft X-ray band (< 15 keV). Si-PIN diode detectors and silicon drift detectors (SDDs), with moderate cooling by means of small Peltier cells, show excellent spectroscopic performance and good detection efficiency below 15 keV. Germanium (Ge) detectors are unsurpassed for high resolution spectroscopy in the hard X-ray energy band (>15 keV) and will continue to be the choice for laboratory-based high performance spectrometers. However, there has been a continuing desire for ambient temperature and compact detectors with the portability and convenience of a scintillator but with a significant improvement in resolution. To this end, numerous high-Z and wide band gap compound semiconductors have been exploited. Among the compound semiconductors, cadmium telluride (CdTe) and cadmium zinc telluride (CdZnTe) are very appealing for hard X-ray detectors and are widely used for the development of spectrometer prototypes for medical and astrophysical applications.

Beside the detector, the readout electronics also plays a key role in the development of high resolution spectrometers. Recently, many research groups have been involved in the design and development of high resolution spectrometers based on semiconductor detectors and on digital pulse processing (DPP) techniques. Due to their lower dead time, higher stability and flexibility, digital systems, based on directly digitizing and processing of detector signals (preamplifier output signals), have recently been favored over analog electronics ensuring high performance in both low and high counting rate environments.

In this chapter, we review the research activities of our group in the development of high throughput and high resolution X-ray spectrometers based on compound semiconductor detectors and DPP systems. First, we briefly describe the physical properties and the signal formation in semiconductor detectors for X-ray spectroscopy. Second, we introduce the main properties and critical issues of a X-ray detection system, highlighting the characteristics of both analog and digital approaches. Finally, we report on the spectroscopic performance of a high resolution spectrometer based on a CdTe detector and a custom DPP system. As an application, direct measurements of mammographic X-ray spectra by using the digital CdTe detection system are also presented.

2. Compound semiconductor detectors

Silicon (Si) and germanium (Ge) are traditional semiconductors used for radiation detectors in a wide range of applications (Knoll, 2000). The growing field of applications stimulated the development of detectors based on compound semiconductors (Knoll, 2000; McGregor & Hermon, 1997; Owens & Peacock, 2004). Compound semiconductors were first investigated as radiation detectors in 1945 by Van Heerden, who used AgCl crystals for detection of alpha particles and gamma rays. The great advantage of compound semiconductors is the possibility to grow materials with a wide range of physical properties (band gap, atomic number, density) making them suitable to almost any application. Interests in radiation detectors operating at room temperature gave rise to development of compound semiconductors with wide band gaps, in comparison to Si and Ge. Moreover, for X-ray and gamma ray detection, compound semiconductors with high atomic number were preferred in order to emphasize photoelectric interaction. It is well known that, among the various interaction mechanisms of X rays with matter, only the photoelectric effect results in the total absorption of the incident energy giving useful information about the photon energy.

Compound semiconductors are generally derived from elements of groups III and V (e.g. GaAs) and groups II and VI (e.g. CdTe) of the periodic table. Besides binary compounds, ternary materials have been also produced, e.g. CdZnTe and CdMnTe. Table 1 reports the physical properties of common compound semiconductors typically used for radiation detection.

Among the compound semiconductors, CdTe and CdZnTe attracted growing interests in the development of X-ray detectors (Del Sordo et al., 2009; Takahashi & Watanabe, 2001). Due to the high atomic number, the high density and the wide band gap (Table 1), CdTe and CdZnTe detectors ensure high detection efficiency, good room temperature performance and are very attractive for X-ray and gamma ray applications. Figure 1(a) shows the linear attenuation coefficients, calculated by using tabulated interaction cross section values (Boone & Chavez, 1996), for photoelectric absorption and Compton scattering of Si (green line), Ge (blu line) and CdTe (red line); as shown in Figure 1(a), photoelectric absorption is the main process up to about 200 keV for CdTe. Figure 1(b) shows the total and photoelectric efficiency for 1 mm thick CdTe detectors, compared with those of traditional semiconductors (Si and Ge with same thickness).

Difficulties in producing detector-grade materials and in growing chemically pure and structurally perfect crystals are the critical issues of CdTe and CdZnTe detectors. In fact, the great potentialities of these compounds has not been exploited for many decades due mainly to the limited commercial availability of high-quality crystals. This situation has changed dramatically during the mid nineties with the emergence of few companies committed to the advancement and commercialization of these materials.

Material	Si	Ge	GaAs	CdTe	$Cd_{0.9}Zn_{0.1}Te$	HgI_2	TlBr
Crystal structure	Cubic	Cubic	Cubic (ZB)	Cubic (ZB)	Cubic (ZB)	Tetragonal	Cubic (CsCl)
Growth method*	C	C	CVD	THM	HPB	VAM	BM
Atomic number	14	32	31, 33	48, 52	48, 30, 52	80, 53	81, 35
Density (g/cm^3)	2.33	5.33	5.32	6.20	5.78	6.4	7.56
Band gap (eV)	1.12	0.67	1.43	1.44	1.57	2.13	2.68
Pair creation energy (eV)	3.62	2.96	4.2	4.4	4.6	4.2	6.5
Resistivity (Ω cm)	10^4	50	10^7	10^9	10^{10}	10^{13}	10^{12}
$\mu_e\tau_e$ (cm^2/V)	> 1	> 1	10^{-4}	10^{-3}	10^{-3}-10^{-2}	10^{-4}	10^{-5}
$\mu_h\tau_h$ (cm^2/V)	~ 1	> 1	10^{-6}	10^{-4}	10^{-5}	10^{-5}	10^{-6}

Table 1. The physical properties of Si, Ge and principal compound semiconductors. The abbreviations are related to the most common growth methods: C = Czochralski, CVD = chemical vapor deposition, THM = traveler heater method, BM = Bridgman method, HPB = high-pressure Bridgman and VAM = vertical ampoule method.

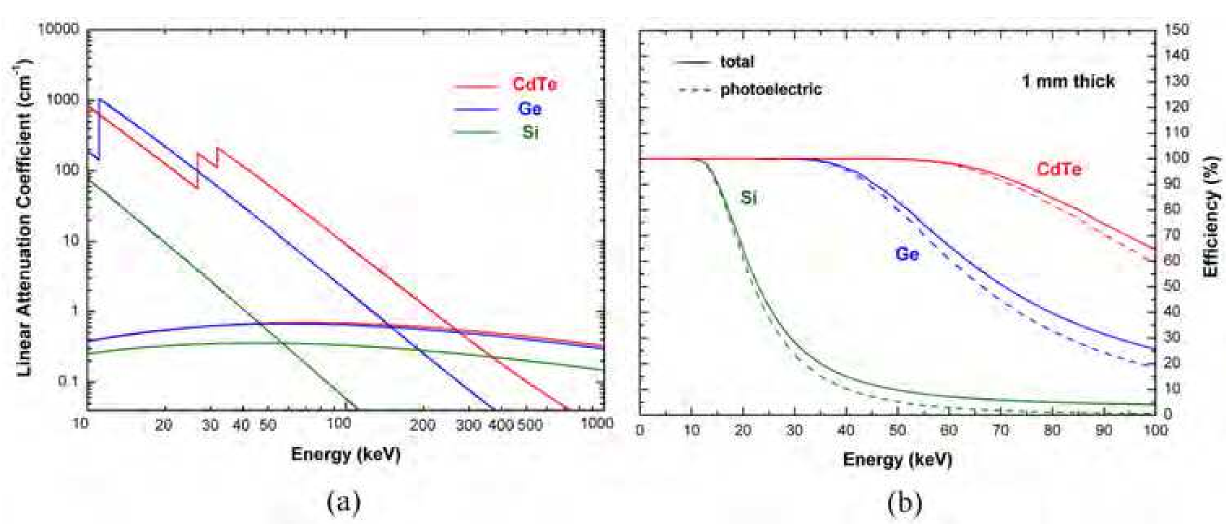

Fig. 1. (a) Linear attenuation coefficients for photoelectric absorption and Compton scattering of CdTe, Si, and Ge. (b) Total and photoelectric efficiency for 1 mm thick CdTe detectors compared with Si and Ge.

3. Principles of operation of semiconductor detectors for X-ray spectroscopy

Semiconductor detectors for X-ray spectroscopy behaves as solid-state ionization chambers operated in pulse mode (Knoll, 2000). The simplest configuration is a planar detector i.e. a slab of a semiconductor material with metal electrodes on the opposite faces of the semiconductor (Figure 2). Photon interactions produce electron-hole pairs in the semiconductor volume through the above discussed interactions. The interaction is a two-step process where the electrons created in the photoelectric or Compton process loose their energy through electron-hole ionization. The most important feature of the photoelectric absorption is that the number of electron-hole pairs is proportional to the photon energy. If E_0 is the incident photon energy, the number of electron-hole pairs N is equal to E_0/w, where w is the average pair creation energy. The generated charge cloud is $Q_0 = e\ E_0/w$. The electrons and holes move toward the opposite electrodes, anode and cathode for electrons and holes, respectively (Figure 2). The movement of the electrons and holes, causes variation ΔQ of induced charge on the electrodes. It is possible to calculate the induced charge ΔQ by the Shockley–Ramo theorem (Cavalleri et al., 1971; Ramo, 1939; Shockley, 1938) which makes use of the concept of a weighting potential φ. The weighting potential is defined as the potential that would exist in the detector with the collecting electrode held at unit potential, while holding all other electrodes at zero potential. According to the Shockley–Ramo theorem, the induced charge by a carrier q, moving from x_i to x_f, is given by:

$$\Delta Q = -q\left[\varphi\ (x_f) - \varphi(x_i)\right] \tag{1}$$

where φ (x) is weighting potential at position x. It is possible to calculate the weighting potential by analytically solving the Laplace equation inside a detector . In a semiconductor, the total induced charge is given by the sum of the induced charges due both to the electrons and holes. For a planar detector, the weighting potential φ of the anode is a linear function of distance x from the cathode:

$$\varphi(x) = \frac{x}{L} \qquad\qquad 0 \le \frac{x}{L} \le 1 \tag{2}$$

where L is the detector thickness. Neglecting charge loss during the transit time of the carriers, the charge induced on the anode electrode by N electron-hole pairs is given by:

$$\begin{gathered} \Delta Q = \Delta Q_h + \Delta Q_e = -\frac{(Ne)}{L}(0-x) + \frac{(Ne)}{L}(L-x) = Ne = Q_0 \\ t > t_h = \frac{x}{\mu_h E} \qquad\qquad t > t_e = \frac{L-x}{\mu_e E} \end{gathered} \tag{3}$$

where t_h and t_e are the transit times of holes and electrons, respectively.

Charge trapping and recombination are typical effects in compound semiconductors and may prevent full charge collection. For a planar detector, having a uniform electric field, neglecting charge de-trapping, the charge collection efficiency (CCE), i.e. the induced charge normalized to the generated charge, is given by the Hecht equation (Hecht, 1932):

$$CCE = \frac{Q}{Q_0} = \left[\frac{\lambda_h}{L}\left(1 - e^{-\frac{x}{\lambda_h}}\right) + \frac{\lambda_e}{L}\left(1 - e^{-\frac{L-x}{\lambda_e}}\right)\right] \quad (4)$$

where $\lambda_h = \mu_h \tau_h E$ and $\lambda_e = \mu_e \tau_e E$ are the mean drift lengths of holes and electrons, respectively. The CCE depends not only on λ_h and λ_e, but also on the incoming photon interaction position. Small λ/L ratios reduce the charge collection and increase the dependence by the photon interaction point. So, the random distribution of the interaction point increases the fluctuations on the induced charge and thus produces peak broadening in the energy spectra. The charge transport properties of a semiconductor, expressed by the hole and electron mobility lifetime products ($\mu_h \tau_h$ and $\mu_e \tau_e$) are key parameters in the development of radiation detectors. Poor mobility lifetime products result in short λ and therefore small λ/L ratios, which limit the maximum thickness and energy range of the detectors. Compound semiconductors, generally, are characterized by poor charge transport properties, especially for holes, due to charge trapping. Trapping centers are mainly caused by structural defects (e.g. vacancies), impurities and irregularities (e.g. dislocations, inclusions). In compound semiconductors, the $\mu_e \tau_e$ is typically of the order of 10^{-5}-10^{-2} cm^2/V while $\mu_h \tau_h$ is usually much worse with values around 10^{-6}-10^{-4} cm^2/V, as reported in Table 1. Therefore, the corresponding mean drift lengths of electrons and holes are 0.2-200 mm and 0.02-2 mm, respectively, for typical applied electric fields of 2000 V/cm.

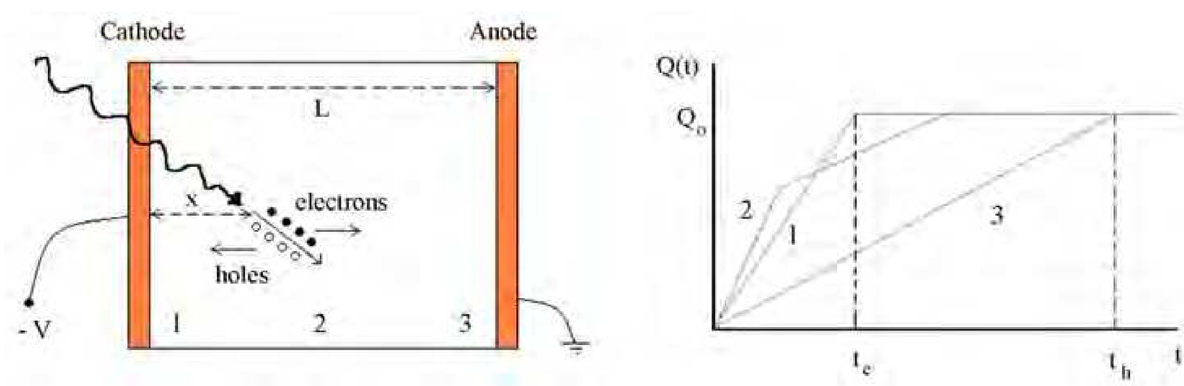

Fig. 2. Planar configuration of a semiconductor detector (left). Electron–hole pairs, generated by radiation, are swept towards the appropriate electrode by the electric field. (right) The time dependence of the induced charge for three different interaction sites in the detector (positions 1, 2 and 3). The fast rising part is due to the electron component, while the slower component is due to the holes.

As pointed out in the foregoing discussions, poor carrier transport properties of CdTe and CdZnTe materials are a critical issue in the development of X-ray detectors. Moreover, the significant difference between the transport properties of the holes and the electrons produces well known effects as spectral distortions in the measured spectra, i.e. peak asymmetries and long tails. To overcome the effects of the poor transport properties of the holes, several methods have been employed (Del Sordo et al., 2009). Some techniques concern the particular irradiation configuration of the detectors. *Planar parallel field* (PPF) is the classical configuration used in overall planar detectors, in which the detectors are irradiated through the cathode electrode, thus minimizing the hole trapping probability. In an alternative configuration, denoted as *planar transverse field* (PTF), the irradiation direction

is orthogonal (transverse) to the electric field. In such configuration different detector thicknesses can be chosen, in order to fit the detection efficiency required, without modifying the inter-electrode distance and then the charge collection properties of the detectors. Several techniques are used in the development of detectors based on the collection of the electrons (single charge carrier sensitive), which have better transport properties than that of the holes. Single charge carrier sensing techniques are widely employed in compound semiconductor detectors by developing careful electrode designs (Frisch-grid, pixels, coplanar grids, strips and multiple electrodes) and by using electronic methods (pulse shape analysis).
As it is well clear from the above discussions, the charge collection efficiency is a crucial property of a radiation detector that affects the spectroscopic performance and in particular the energy resolution. High charge collection efficiency ensures good energy resolution which also depends by the statistics of the charge generation and by the noise of the readout electronics. Generally, the energy resolution of a radiation detector, estimated through the full-width at half maximum (FWHM) of the full-energy peaks, is mainly influenced by three contributes:

$$\Delta E = \sqrt{(2.355)^2 (F \cdot E_0 \cdot w) + \Delta E_{el}{}^2 + \Delta E_{coll}{}^2} \tag{5}$$

The first contribute is the Fano noise due to the statistics of the charge carrier generation. In compound semiconductors, the Fano factor F is much smaller than unity (0.06-0.14). The second contribute is the electronic noise which mainly depends on the readout electronics and the leakage current of the detector, while the third is the contribute of the charge collection process.

4. Electronics for high resolution spectroscopy: The digital pulse processing (DPP) approach

Nowadays, the dramatic performance improvement of the analog-to-digital converters (ADC) stimulated an intensive research and development on digital pulse processing (DPP) systems for high resolution X-ray spectroscopy. The availability of very fast and high precision digitizers has driven physicists and engineers to realize electronics in which the analog-to-digital conversion is performed as close as possible to the detector. This approach is reversed with respect to more traditional electronics which were made out of mainly analog circuits with the A/D conversion at the end of the chain. Figure 3 shows the simplified block diagrams of analog and DPP electronics for X-ray detectors. In a typical analog electronics, the detector signals are amplified by a charge sensitive preamplifier (CSP), shaped and filtered by an analog shaping amplifier and finally processed by a multichannel analyzer (MCA) to generate the energy spectrum. In a DPP system, the preamplifier output signals are directly digitized by an ADC and so processed by using digital algorithms. A DPP system leads to better results than the analog one, mainly due to (i) stability, (ii) flexibility and (iii) higher throughput (i.e. the rate of the useful counts in the energy spectrum). With regard to the improved stability of a DPP system, the direct digitizing of the detector signals minimizes the drift and instability normally associated with analog signal processing. In terms of flexibility, it is possible to implement complex algorithms, that are not easily implementable through a traditional analog approach, for adaptive processing and optimum filtering. Moreover, a DPP analysis require considerably

less overall processing time than the analog one ensuring lower dead time and higher throughput, very important under high rate conditions. The dead time of an analog system is mainly due to the pulse processing time of the shaper and to the conversion time of MCA. The pulse processing time is generally related to the temporal width of the pulse which depends on the shaping time constant of the shaper and can be described through the well known paralyzable dead time model (Knoll, 2000). The MCA dead time, generally described by nonparalyzable dead time model (Knoll, 2000), is often the dominant contributor to overall dead time. In a DPP system there is no additional dead time associated with digitizing the pulses and so the equivalent to MCA dead time is zero. Therefore the overall dead time of a digital system is generally lower than that of the analog one.
An another positive aspect of the DPP systems regards the possibility to perform off-line analysis of the detector signals: *since that signals are captured, more complex analyses can be postponed until the source event has been deemed interesting*.

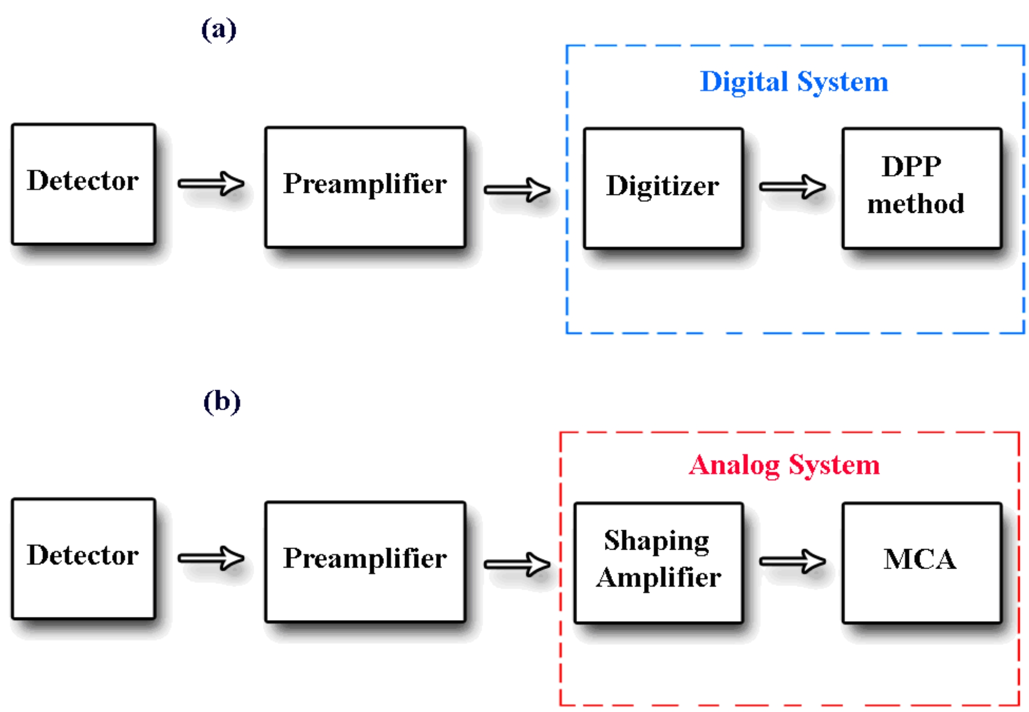

Fig. 3. Simplified block diagrams of (a) digital and (b) analog detection systems.

5. A digital CdTe X-ray spectrometer for both low and high counting rate environments

In this section, we report on the spectroscopic performance of a CdTe detector coupled to a custom DPP system for X-ray spectroscopy. We first describe the main characteristics of the detector and the DPP system and then we present the results of the characterization of the overall detection system at both low (200 cps) and high photon counting rates (up to 800 kcps) by using monoenergetic X-ray sources (^{109}Cd, ^{152}Eu, ^{241}Am, ^{57}Co) and a nonclinical X-ray tube with different anode materials (Ag, Mo). This work was carried out in the sequence of previously developed DPP systems (Abbene et al., 2007, 2010a, 2010b, 2011; Gerardi et al., 2007) with the goal of developing a digital spectrometer based on DPP techniques and characterized by high performance both at low and high photon counting rate environments.

5.1 CdTe detector

The detector is based on a thin CdTe crystal (2 x 2 x 1 mm^3), wherein both the anode (indium) and the cathode (platinum) are planar electrodes covering the entire detector surface. The Schottky barrier at the In/CdTe interface ensures low leakage current even at high bias voltage operation (400 V), thus improving the charge collection efficiency. The thickness of the detector guarantees a very good photon detection efficiency (~99%) up to 40 keV. A Peltier cell cools both the CdTe crystal and the input FET of the charge sensitive preamplifier (A250, Amptek, U.S.A.) at a temperature of -20 °C. Cooling the detector reduces the leakage current, allowing the application of higher bias voltages to the electrodes; moreover, cooling the FET increases its transconductance and reduces the electronic noise. The detector, the FET and the Peltier cooler are mounted in a hermetic package equipped with a light-vacuum tight beryllium window (modified version of Amptek XR100T-CdTe, S/N 6012). To increase the maximum counting rate of the preamplifier, a feedback resistor of 1 GΩ and a feedback capacitor of 0.1 pF were used. The detector is equipped with a test input to evaluate the electronic noise.

5.2 Digital pulse processing system

The DPP system consists of a digitizer and a PC wherein the digital analysis of the detector pulses (preamplifier output pulses) was implemented. The detector signals are directly digitized by using a 14-bit, 100 MHz digitizer (NI5122, National Instruments). The digital data are acquired and recorded by a Labview program on the PC platform and then processed off-line by a custom digital pulse processing method (C++ coded software) developed by our group. The analysis time is about 3 times the acquisition time. The DPP method, implemented on the PC platform, performs a height and shape analysis of the detector pulses. Combining fast and slow shaping, automatic pole-zero adjustment, baseline restoration and pile-up rejection, the digital method allows precise pulse height measurements both at low and high counting rate environments. Pulse shape analysis techniques (pulse shape discrimination, linear and non linear pulse shape corrections) to compensate for incomplete charge collection were also implemented. The digitized pulses are shaped by using the classical single delay line (SDL) shaping technique (Knoll, 2000). Each shaped pulse is achieved by subtracting from the original pulse its delayed and attenuated fraction. The attenuation of the delayed pulse allows to eliminate the undesirable undershoot following the shaped pulse, i.e. acting as pole-zero cancellation. For a single digitized pulse, consisting of a defined number of samples, this operation can be represented by the following equation:

$$V^{shaped}(nT_s) = V^{preamp}(nT_s) - \left[V^{preamp}(nT_s - n_d T_s)\right] \cdot A \tag{6}$$

where T_s is the ADC sample period, $n_d\ T_s = T_d$ is the delay time, A is the attenuation coefficient, $V^{shaped}(nT_s)$ is the shaped sample at the discrete time instant nT_s and $V^{preamp}(nT_s)$ is the preamplifier output sample at the discrete time instant nT_s. The width of each shaped pulse is equal to $T_d + T_p$, wherein T_p is the peaking time of the related preamplifier output pulse.

Our DPP method is characterized by two shaping modes: a "*fast*" SDL shaping mode and a "*slow*" SDL shaping mode, operating at different delay times. The "*fast*" shaping operation, characterized by a short delay time $T_{d,\,fast}$, is optimized to detect the pulses and to provide a pile-up inspection. If the width of the shaped pulses exceeds a maximum width threshold then the pulse is classified as representative of pile-up events; whenever it is possible, each overlapped event is recognized through a peak detection analysis. Obviously, these events are not analyzed by the "*slow*" shaping procedure. The delay time of the "*fast*" shaping operation is a dead time for the DPP system (paralyzable dead time) and it must be as small as possible, depending of detector and ADC characteristics. With regard to the paralyzable model, the true photon counting rate n is related to the measured photon counting rate m through the following equation (Knoll, 2000):

$$m = n \cdot \exp\left[-nT_{d,fast}\right] \tag{7}$$

It is possible to evaluate the true rate n from the measured rate m by solving the equation (7) iteratively. The DPP system, through the "*fast*" shaping operation, gives the estimation of the true rate n through the equation (7) and the measured rate m. We used $T_{d,\,fast}$ = 50 ns.
The "*slow*" shaping operation, which has a longer delay time $T_{d,\,slow}$ than the "*fast*" one, is optimized to shorten the pulse width and minimize the ballistic deficit. To obtain a precise pulse height measurement, a convolution of the shaped pulses with a Gaussian function was performed. The slow delay time $T_{d,\,slow}$ acts as the shaping time constant of an analog shaping amplifier: the proper choice depends on the peaking time of the preamplifier pulses, the noise and the incoming photon counting rate.
To ensure good energy resolution also at high photon counting rates, a standard detection system is typically equipped with a baseline restorer which minimize the fluctuations of the baseline. The digital method performs a baseline recovery by evaluating the mean value of the samples, within a time window equal to $T_{d,\,slow}/2$, before and after each shaped pulse. This operation sets a minimum time spacing between the pulses equal to $T_a = 2 \cdot T_{d,\,slow} + T_p$ for which no mutual interference must exist in the baseline measurement. The minimum time spacing T_a is used to decide whether the events must be discarded, in particular if the time spacing does not exceed T_a the two events are rejected. It is clear that a $T_{d,\,slow}$ value too long reduces the number of the counts in the measured spectrum (analyzed events) and its optimum value is the best compromise between the required energy resolution and throughput. The time T_a is paralyzable dead time for the *slow* shaping operation. Both *fast* and *slow* procedures gave consistent values of the incoming photon counting rate.

5.2.1 Pulse shape discrimination

A pulse shape discrimination (PSD) technique was implemented in our DPP system by analyzing the peaking time distribution of the pulses and their correlations with the energy spectra. Pulse shape discrimination, first introduced by Jones in 1975 (Jones & Woollam, 1975), is a common technique to enhance spectral performance of compound semiconductor detectors. Generally, this technique is based on the selection of a range of peaking time values of the pulses that are less influenced of incomplete charge collection. As previously discussed, incomplete charge collection, mainly due to the poor transport properties of the holes, is a typical drawback of compound semiconductor detectors, producing long tailing and asymmetry in the measured spectra. As well known, the pulses mostly influenced by the hole contribution are generally characterized by longer peaking times. These effects are more prominent increasing the energy of radiation (i.e. the depth of interaction of radiation); the events, with a greater depth of interaction, take place close to the anode electrode producing pulses mostly due to the hole transit.

To perform the pulse shape analysis, we carried out the measurement of the peaking time of the analyzed pulses. We first evaluate the rise time of the pulses, i.e. the interval between the times at which the shaped pulse reaches 10% and 90% of its height (after baseline restoration). The times, corresponding to the exact fractions (10% and 90%) of the pulse height, are obtained through a linear interpolation. We estimate the peaking time equal to 2.27 times the rise time (i.e. about five times the time constant). Due to the precise measurement of the pulse height-baseline and interpolation, the method allows fine peaking time estimations (with a precision of 2 ns) both at low and high photon counting rates.
Figure 4(a) shows the pulse peaking time distribution of ^{57}Co events measured with the CdTe detector. The distribution has an asymmetric shape and suffers from a tail, which is attributed to the slow peaking time events. The correlation between the peaking time and the height of the pulses is pointed out by the bi-parametric distribution (^{57}Co source), shown in Figure 4(b). It is clearly visible that for longer peaking times, the photopeak shifts to lower energies, as expected. This distribution is very helpful to better understand the tailing in the measured spectra and implement correction methods.

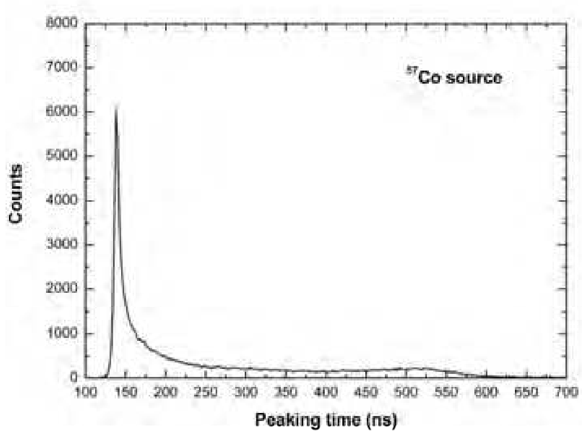

(a)

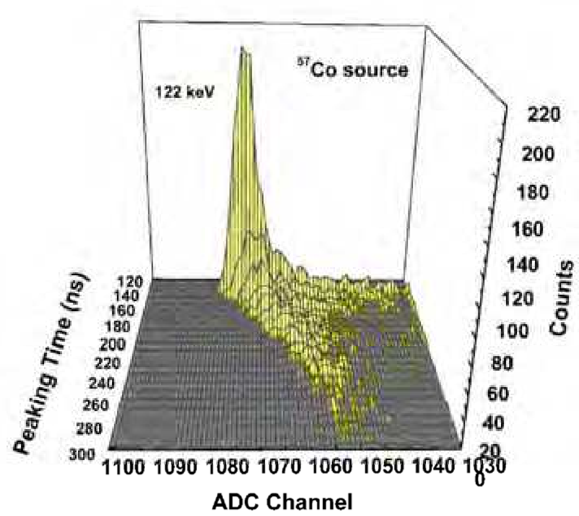

(b)

Fig. 4. (a) Pulse peaking time distribution of the CdTe detector (^{57}Co source). The peaking time is equal to 2.27 times the rise time of the pulses. (b) 3D plot of ^{57}Co spectra measured for different peaking time values (bi-parametric distribution).

As proposed by Sjöland in 1994 (Sjöland & Kristiansson, 1994) pulse shape discrimination can also be used to minimize peak pile-up events, i.e. overlapped preamplified pulses within the peaking time that are not detectable through the "*fast*" shaping operation. Because the shape (peaking time) of a peak pile-up pulse differs from that of a pulse not affected by pile-up, analyzing the measured spectra at different peaking time regions (PTRs) in the peaking time distribution is helpful to reduce peak pile-up. Figure 5(a) shows some selected PTRs in the peaking time distribution of the pulses from the ^{109}Cd source (at 820 kcps), while in Figure 5(b) are shown the ^{109}Cd spectra for each PTR. These results point out the characteristics of the peak pile-up events, which have a longer peaking time than the correct events, and then the potentialities of the PSD technique to minimize these spectral distortions.

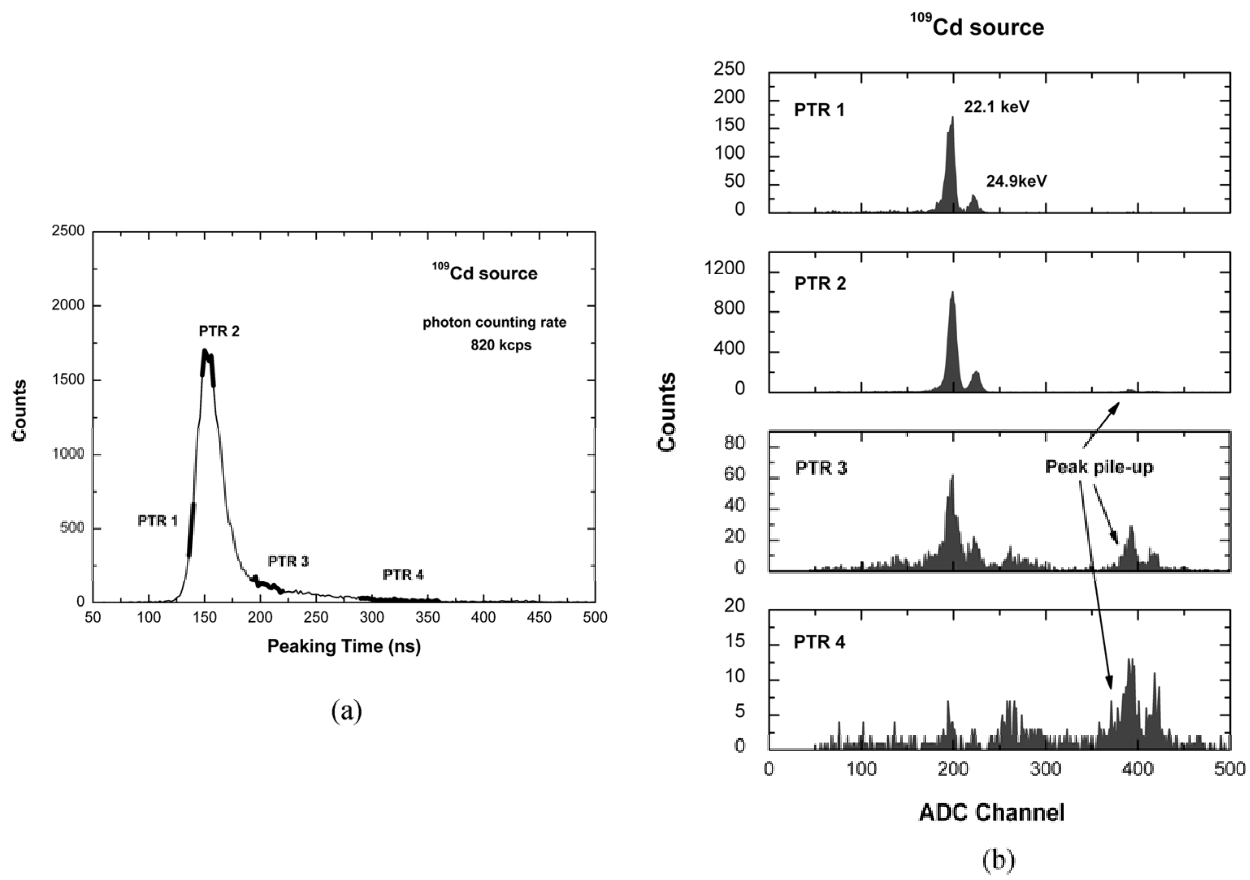

Fig. 5. (a) Pulse peaking time distribution of the CdTe detector (^{109}Cd source) at a photon counting rate of 820 kcps; the selected peaking time regions (PTRs) are also visible. (b) ^{109}Cd spectra for the selected PTRs (820 kcps). It is evident that the peak-pile events are characterized by longer peaking times than the correct events.

5.2.2 Linear and non linear pulse shape corrections

Despite the potentiality of the PSD technique, the choice of the optimum peaking time region is a trade-off between the energy resolution and the counts in the measured spectrum. The strong correlation between the peaking time and the height of the pulses, as shown in Figure 4(b), opens up the possibility of charge loss correction.

Parallel to the PSD technique, we implemented linear and non linear pulse shape correction (PSC) methods in our DPP system, based on the measurement of both the peaking time and the height of the pulses. As introduced by Keele et al. (Keele et al., 1996), the method corrects all pulses to a hypothetical zero peaking time. The method requires a preliminary calibration procedure, strictly depending on the characteristics of the detector, based on the analysis of the behaviour of the centroid of photopeaks versus the peaking time. Figure 6(a) shows the photopeak centroid vs. the peaking time values for some photopeaks of the measured spectra (^{109}Cd, ^{152}Eu, ^{241}Am and ^{57}Co). We analyzed the photopeak centroid shift by using the following linear function:

$$E_{\det} = m_E \cdot T_p + E_{cor} \tag{8}$$

where E_{det} is the photopeak centroid, m_E is the slope of the linear function, T_p is the peaking time and E_{cor} is the corrected centroid at zero peaking time. The corrected centroid, E_{cor}, is the result of correcting E_{det} to an ideal point of zero peaking time and it is the desired height for a pulse. It is interesting to note that both the slope m_E and E_{cor} are linear functions of the photon energy E, as shown in Figures 6(b) and 6(c).

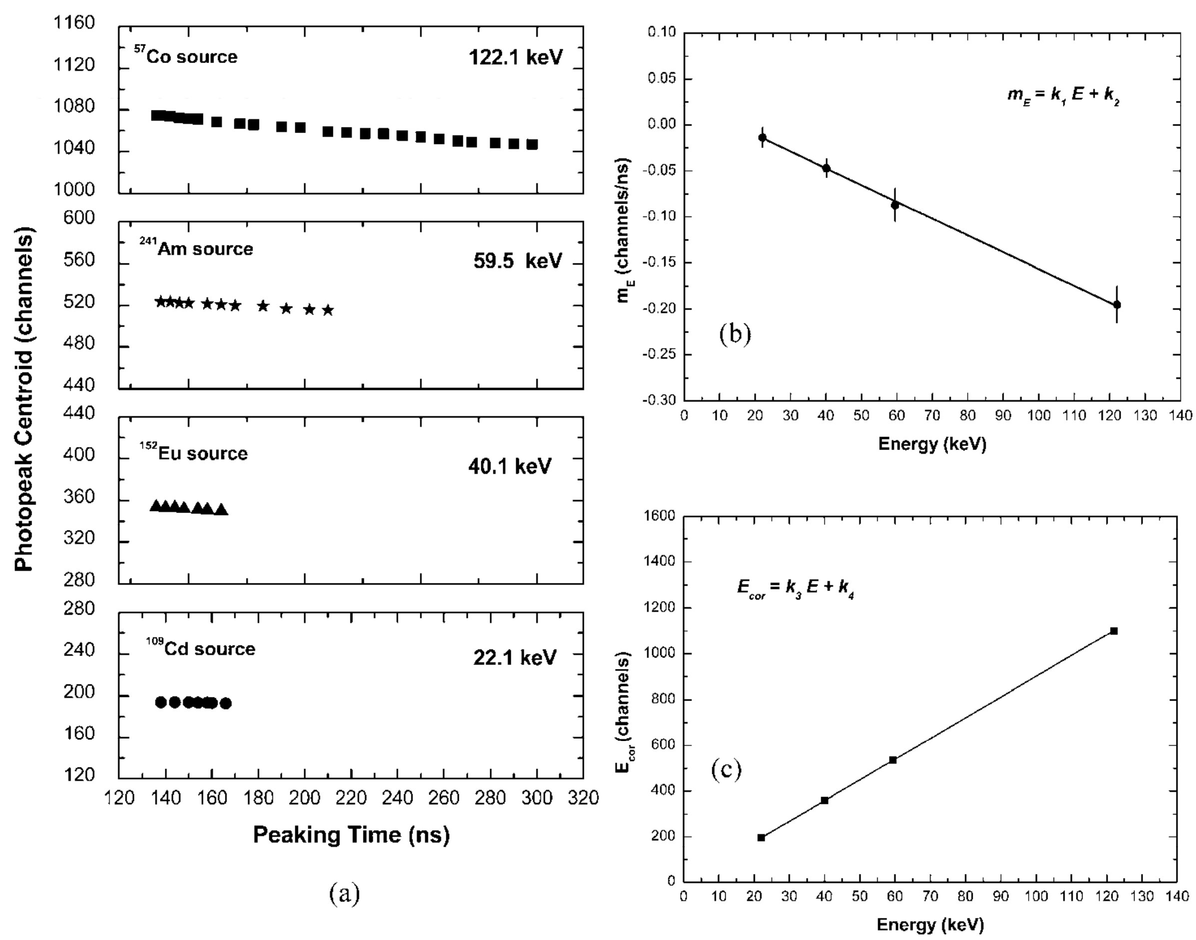

Fig. 6. (a) Photopeak centroid vs. the peaking time values for some photopeaks of the measured spectra (^{109}Cd, ^{152}Eu, ^{241}Am and ^{57}Co). (b) Slope m_E and (c) corrected centroid E_{cor} vs. the radiation energy.

The fitting equations are:

$$m_E = k_1 \cdot E + k_2 \tag{9}$$

$$E_{cor} = k_3 \cdot E + k_4 \tag{10}$$

where k_1, k_3 and k_2 , k_4 are the slopes and the y-intercepts of the linear functions, respectively. Combining the equations (9) and (10), yields:

$$m_E = \frac{k_1}{k_3} \cdot (E_{cor} - k_4) + k_2 \tag{11}$$

i.e.:

$$m_E = A \cdot E_{cor} + B \tag{12}$$

with:

$$A = \frac{k_1}{k_3} \qquad B = \frac{k_2 \cdot k_3 - k_1 \cdot k_4}{k_3}. \tag{13}$$

Combining the equations (8) and (12), yields:

$$E_{cor} = \frac{(E_{\det} - B \cdot T_p)}{1 + A \cdot T_p} \tag{14}$$

By using equation (14) is possible to adjust the pulse height E_{det} of a pulse through the knowledge of the bi-parametric distribution and of the constants A and B obtained by the calibration procedure.
We also implemented a non linear pulse shape correction method, by using the following function:

$$E_{\det} = n_E \cdot T_p^{\,2} + m_E \cdot T_p + E_{cor} \tag{15}$$

where the coefficients n_E, m_E and E_{cor} are yet linear functions of the photon energy E:

$$n_E = k_5 \cdot E + k_6 \tag{16}$$

$$m_E = k_7 \cdot E + k_8 \tag{17}$$

$$E_{cor} = k_9 \cdot E + k_{10} \tag{18}$$

So, combining the equations (16), (17), (18) with (15) yields:

$$E_{cor} = -\frac{- E_{\det} \cdot k_9 + (k_9 \cdot k_8 - k_{10} \cdot k_7) \cdot T_p + (k_9 \cdot k_6 - k_{10} \cdot k_5) \cdot T_p^{\,2}}{k_9 + k_7 \cdot T_p \ + k_5 \cdot T_p^{\,2}} \tag{19}$$

The bi-parametric correction method presents an important limitation: it is only applicable to pure photoelectric interactions, i.e. when the energy of each incident photon is deposited at a single point in the detector. If the photon Compton scatters at one depth in the detector and then undergoes photoelectric absorption at a second depth, the height-peaking time relationship can vary from that due to a single interaction. For high atomic number compound semiconductors, such as CdTe and CdZnTe, photoelectric absorption is the main process up to about 200 keV (Del Sordo et al., 2009).

5.3 Spectroscopic characterization

To investigate on the spectroscopic performance of the system, we used X-ray and gamma ray calibration sources (^{109}Cd: 22.1, 24.9 and 88.1 keV; ^{241}Am: 59.5, 26.3 keV and the Np L X-ray lines between 13 and 21 keV; ^{152}Eu: 121.8 keV and the Sm K lines between 39 and 46 keV;

^{57}Co: 122.1, 136.5 keV and the W fluorescent lines, $K_{\alpha1}$=59.3 keV, $K_{\alpha2}$=58.0 keV, $K_{\beta1}$=67.1 keV, $K_{\beta3}$=66.9 keV, produced in the source backing). The 14 keV gamma line (^{57}Co) is shielded by the source holder itself. For high rate measurements, we also used another ^{241}Am source, with the Np L X-ray lines shielded by the source holder. To obtain different rates (up to 820 kcps) of the photons incident on the detector (through the cathode surface), we changed the irradiated area of the detector by using collimators (Pb and W) with different geometries.
To better investigate on the high-rate performance of the system, we also performed the measurement of Mo-target X-ray spectra at the "Livio Scarsi" Laboratory (LAX) located at DIFI (Palermo).

(a) (b)

Fig. 7. (a) An overview of the LAX facility. (b) The detector chamber located at 10.5 m from the X-ray tube; the detection system was mounted on a XYZ microtranslator system.

The facility is able to produce X-ray beams with an operational energy range of 0.1–60 keV (tube anodes: Ag, Co, Cr, Cu, Fe, Mo, W), collimated on a length of 10.5 m with a diameter at full aperture of 200 mm (Figure 7). In this work, we used Mo and Ag targets. No collimators were used for these measurements. To characterize the spectroscopic performance of the system, we evaluated, from the measured spectra, the *energy resolution* (*FWHM*) and the *FW.25M to FWHM ratio,* defined in agreement with the IEEE standard (IEEE Standard, 2003). We also evaluated the area of the energy peaks (photopeak area) through the *high side area* (*HSA*) (IEEE Standard, 2003), i.e. the area between the peak center line and the peak's high-energy toe; the photopeak area was calculated as twice the *HSA*. The measured spectra were analyzed by using a custom function model, which takes into account both the symmetric and the asymmetric peak distortion effects (Del Sordo et al., 2004). Statistical errors on the spectroscopic parameters with a confidence level of 68% were associated.

5.3.1 Low count rate performance

In this paragraph we present the performance of the system at low photon counting rate (200 cps), by using PSD, linear and non linear PSC techniques. We first used the PSD technique looking for the best performance despite the high reduction of the photopeak area (about 90%). With regard to the PSD technique, we obtained the following results: energy resolution (*FWHM*) of 2.05 %, 0.98 % and 0.68 % at 22.1, 59.5 and 122.1 keV, respectively. Figure 8 shows the measured ^{241}Am and ^{57}Co spectra using PSD and no PSD techniques. To better point out the spectral improvements of the PSD technique, we report in Figures 8(b) and 8(d) a zoom of the 59.5 and 122.1 keV photopeaks, normalized to the photopeak centroid counts. As widely shown in several works, PSD produced a strong reduction of peak asymmetry and tailing in the measured spectra: the 122.1 keV photopeak of ^{57}Co spectrum, after PSD, is characterized by an energy resolution improvement of 57 % and low tailing; the *FW.25M to FWHM ratio* is reduced up to 1.46, quite close to the ideal Gaussian ratio ($FW.25M/FWHM_{Gaussian}$=1.41).

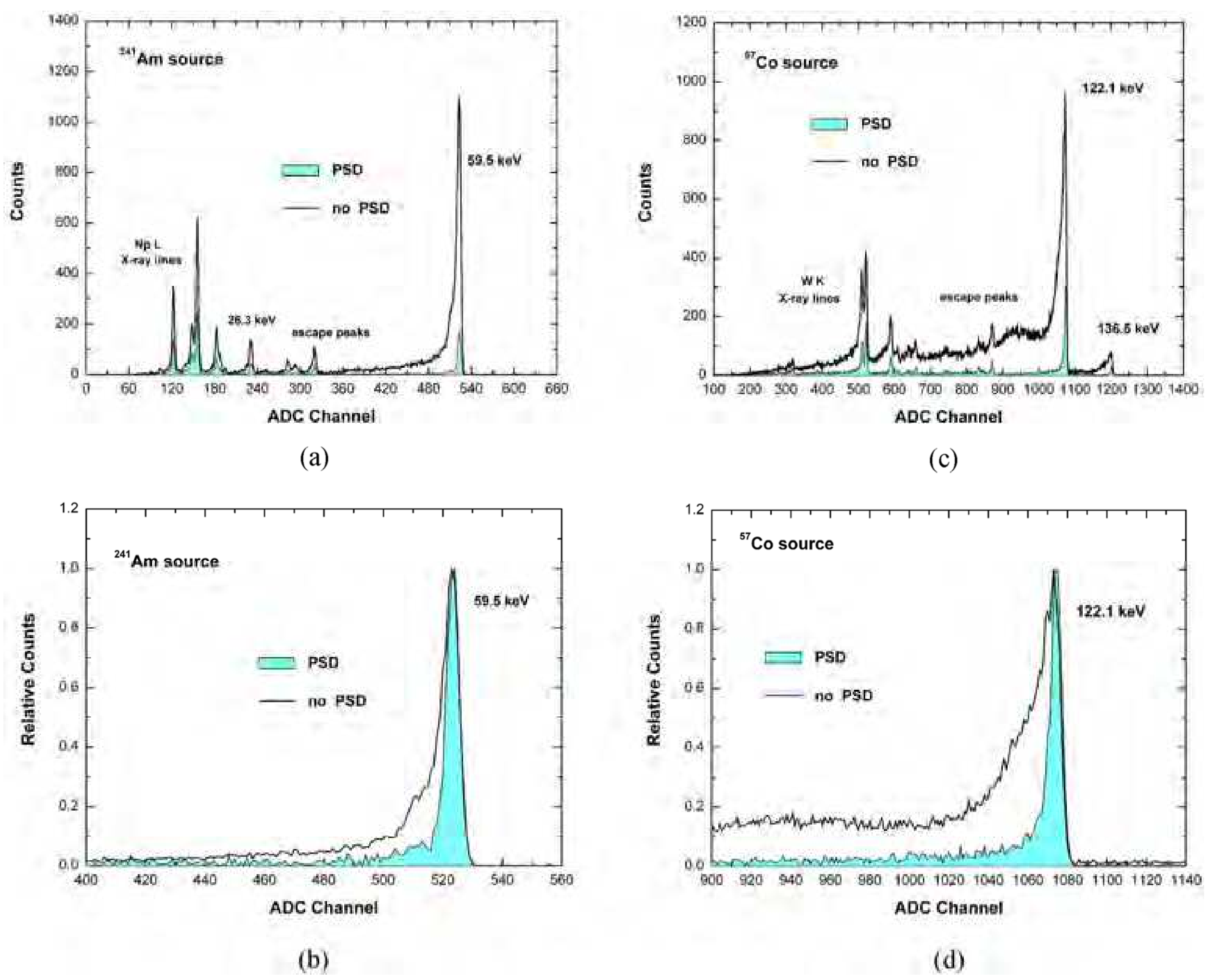

Fig. 8. Measured (a) ^{241}Am and (c) ^{57}Co spectra using PSD and no PSD techniques. After PSD, we obtained an energy resolution of 0.98 % and 0.68 % *FWHM* at 59.5 keV and 122.1 keV, respectively. Zoom of the (b) 59.5 and (d) 122.1 keV photopeaks, normalized to the photopeak centroid counts.

The reduction of trapping effects allows to use some semi-empirical models of the energy resolution function that can be used to estimate some characteristic parameters of compound semiconductors, such as the Fano factor *F* and the average pair creation energy

w. For low trapping, the energy resolution, as proposed by Owens (Owens & Peacock, 2004), can be described by the following equation:

$$\Delta E = \sqrt{(2.355)^2 (F \cdot E \cdot w) + \Delta E_{el}^{\ 2} + a \cdot E^b} \tag{20}$$

where a and b are semi-empirical constants that can be obtained by a best-fit procedure. The equation (20) could be used to estimate the Fano factor F and the average pair creation energy w. In our case, we used a tabulated value of w (4.43 eV) and obtained F, a and b by a best-fit procedure; we also measured the energy resolution of the 17.77 keV Np L X-ray line to obtain almost one degree of freedom (*dof*).
Best fitting equation (20) to the measured energy resolution points (with no PSD) resulted in a bad fit, due to the high trapping contribute. We obtained a good fit with the measured data points after PSD [$\chi^2/dof = 1.21$; $dof = 1$)], as shown in Figure 9.

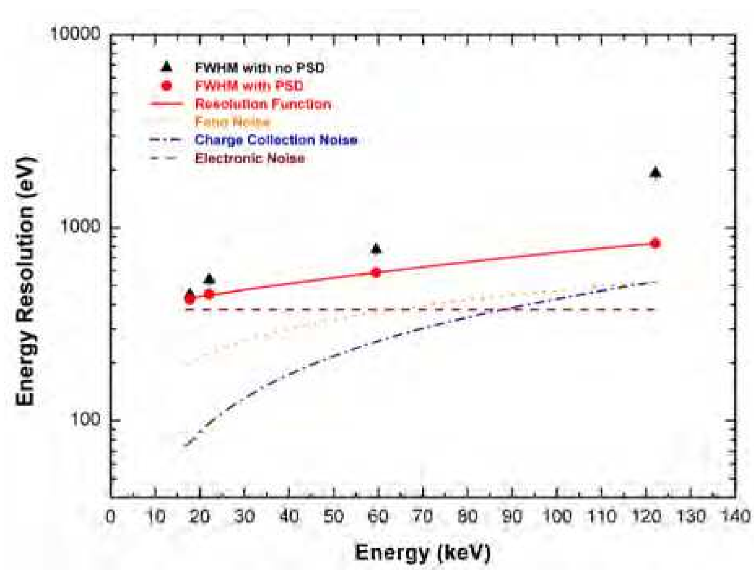

Fig. 9. Energy resolution (*FWHM*) using no PSD and PSD techniques. The solid line is the best-fit resolution function (equation 20). The components of the energy resolution are also shown: the noise due to carrier generation or Fano noise, the electronic noise and charge collection or trapping noise.

The fitted value for the Fano factor (0.09±0.03) is in agreement with the literature values (Del Sordo et al., 2009). Figure 9, also, shows the individual components of the energy resolution (after PSD). It is clearly visible that electronic noise (dashed line) dominates the resolution function below 60 keV, whereas Fano noise (dotted line) dominates the charge collection noise (dot-dashes line) within the overall energy range (up to 122 keV). After PSD, the charge collection noise is mainly due to electron trapping and diffusion. We stress that this analysis was performed in order to better point out the performance enhancements of the PSD technique and not for precise measurements of Fano factor. Nevertheless, the potentialities of the technique for precise Fano factor estimations are well evident: It would be sufficient to measure a greater number of monoenergetic X-ray lines to ensure more precise Fano factor estimations.
Table 2 shows the performance of the detector with no correction, after PSD, linear and non linear PSC.

Spectroscopic parameter	Energy (keV)				
	59.5				
	No correction	PSD 100 ≤PTR≤ 170 ns	Linear PSC and PSD 100 ≤PTR≤ 178 ns	Linear PSC	Non linear PSC
Energy resolution *FWHM* (%)	1.29 ± 0.05	1.19 ± 0.04	1.12 ± 0.04	1.19 ± 0.04	1.17 ± 0.04
FW.25M to FWHM ratio (Gaussian ratio 1.41)	2.00 ± 0.05	1.53 ± 0.05	1.51 ± 0.05	1.70 ± 0.04	1.64 ± 0.05
Percentage deviation of photopeak area (%)	0	0	0	+5	+10
Percentage deviation of total counts (%)	0	-23	-20	0	0
	122.1				
	No correction	PSD 100 ≤PTR≤ 198 ns	Linear PSC and PSD 100 ≤PTR≤ 180 ns	Linear PSC	Non linear PSC
Energy resolution *FWHM* (%)	1.58 ± 0.05	1.21 ± 0.07	0.73 ± 0.04	0.89 ± 0.04	0.87 ± 0.04
FW.25M to FWHM ratio (Gaussian ratio 1.41)	2.30 ± 0.05	1.69 ± 0.07	1.65 ± 0.07	1.93 ± 0.04	1.89 ± 0.06
Percentage deviation of photopeak area (%)	0	0	0	+51	+65
Percentage deviation of total counts (%)	0	-44	-50	0	0

Table 2. Spectroscopic results for the CdTe detector at low photon counting rate (200 cps) using pulse shape analysis techniques. Changes of the photopeak area and total counts are calculated respect to the spectra with no correction. The photopeak area was calculated as twice the *HSA*. We used $T_{d,\,slow}$= 15 μs.

We first used (i) the PSD technique selecting the PTR which produced no reduction of the photopeak area, (ii) we applied both linear PSC and PSD to obtain no reduction of the photopeak area, and finally (iii) we applied both linear and non linear PSC techniques to all peaking time values obtaining no reduction of the total counts. Figure 10(a) shows the enhancements in ^{57}Co spectra after linear PSC and the PSD techniques, without any photopeak area reduction. Figure 10(b) shows the enhancements in ^{57}Co spectra after non linear PSC, applied to all peaking time values (with no reduction of the total counts). No spectral improvements are obtained in ^{109}Cd spectrum with the PSC methods.
Despite the similar results for linear and non linear corrections, the implementation of the non linear correction opens up to the possibility for charge collection compensation for thicker detectors wherein hole trapping effects are more severe. We stress as the flexibility of the digital pulse processing approach also allows the easy implementation of more complicated correction methods for the minimization of incomplete charge collection.

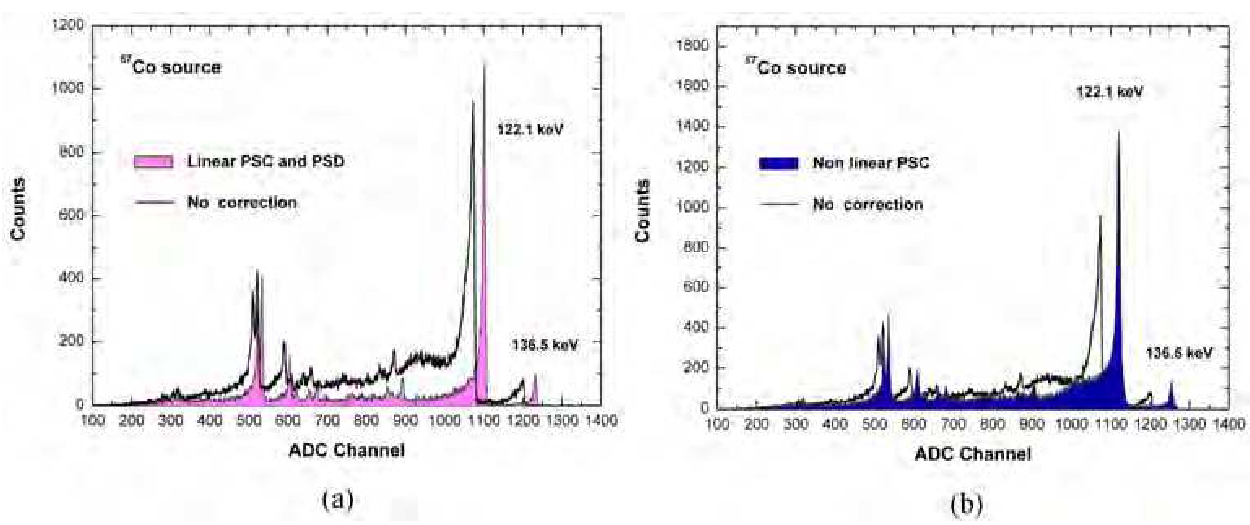

Fig. 10. (a) Measured ^{57}Co spectra with no correction and using both linear PSC and PSD. The linear PSC was applied to a selected PTR which ensured no photopeak area reduction. After linear PSC, we obtained an energy resolution of 0.73% *FWHM* at 122.1 keV. (b) Measured ^{57}Co spectra with no correction and using non linear PSC. The non linear PSC was applied to all peaking time values obtaining no reduction of the total counts. After non linear PSC, we obtained an energy resolution of 0.87% *FWHM* at 122.1 keV.

5.3.2 High count rate performance

Figure 11 shows the performance of the detection system (with $T_{d,\ slow}$= 3 μs), irradiated with the ^{109}Cd source, at different photon counting rates (up to 820 kcps). The throughput of the system (i.e. the rate of the events in the spectrum or the rate of the analyzed events by the "*slow*" pulse shaping), the 22.1 keV photopeak centroid and the energy resolution (FWHM) at 22.1 keV were measured. The photopeak centroid shift was less than 1 % and low energy resolution worsening characterized the system. Despite the low throughput of the system, it is possible to measure the input photon counting rate through the "*fast*" pulse shaping. The system, through both "*slow*" and "*fast*" pulse shaping is able to determine the input count rate and the energy spectrum with high accuracy and precision even at high photon counting rates.

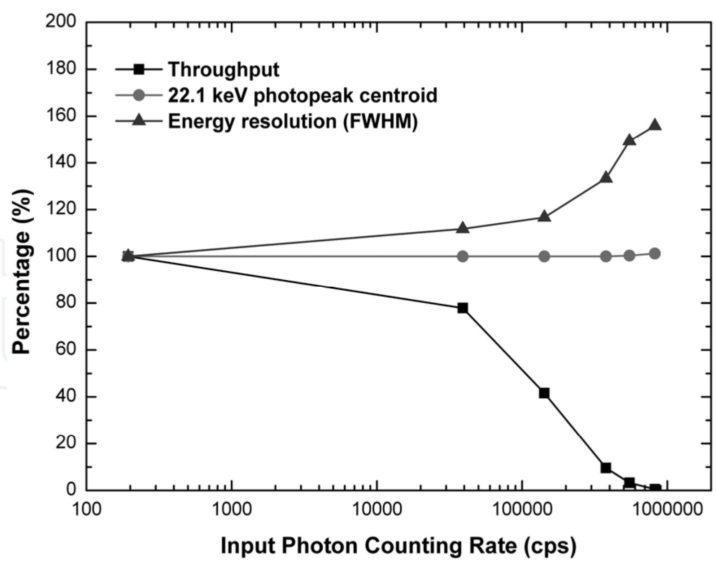

Fig. 11. Performance of the detection system, irradiated with a ^{109}Cd source: throughput, 22.1 keV photopeak centroid and energy resolution (*FWHM*) at 22.1 keV at different input photon counting rates .

Figure 12 shows the measured ^{109}Cd spectra at (a) 200 cps with no correction, (b) at 820 kcps with no correction and (c) at 820 kcps after PSD (100 ≤PTR≤ 148 ns). The results (summarized in Table 3) highlight the excellent high rate capability of our digital system. Moreover, PSD allowed a strong reduction (96%) of the number of peak pile-up events in the measured spectrum, as shown in Figure 12(c).

	Energy			
	22.1 keV		59.5 keV	
	No correction	PSD 100≤PTR≤148 ns	No correction	Linear PSC and PSD 100≤PTR≤154 ns
Energy resolution *FWHM* (%)	4.77 ± 0.04	4.52 ± 0.04	2.12 ± 0.04	1.87 ± 0.04
Total rate (kcps)	820	820	255	255
Analyzed rate or Spectrum rate (kcps)	4.4	1.1	53.5	28.4

Table 3. Spectroscopic results from high rate measurements. The energy resolution at low rate 200 cps is (with $T_{d,\ slow}$= 3 µs): 3.1% at 22.1 keV and 1.9% at 59.5 keV. Both PSD and linear PSC give a peak pile-up reduction of 96%.

High-rate ^{241}Am spectrum measurements (Figures 12(d), (e), (f)) also show as both PSD and linear PSC can be used for compensation of charge trapping and peak pile-up. With regard to ^{241}Am spectra, we first minimized peak pile-up (with a reduction of about 96%) by selecting a proper PTR (100 ≤PTR≤ 154 ns) and then we applied the linear PSC in the selected PTR.

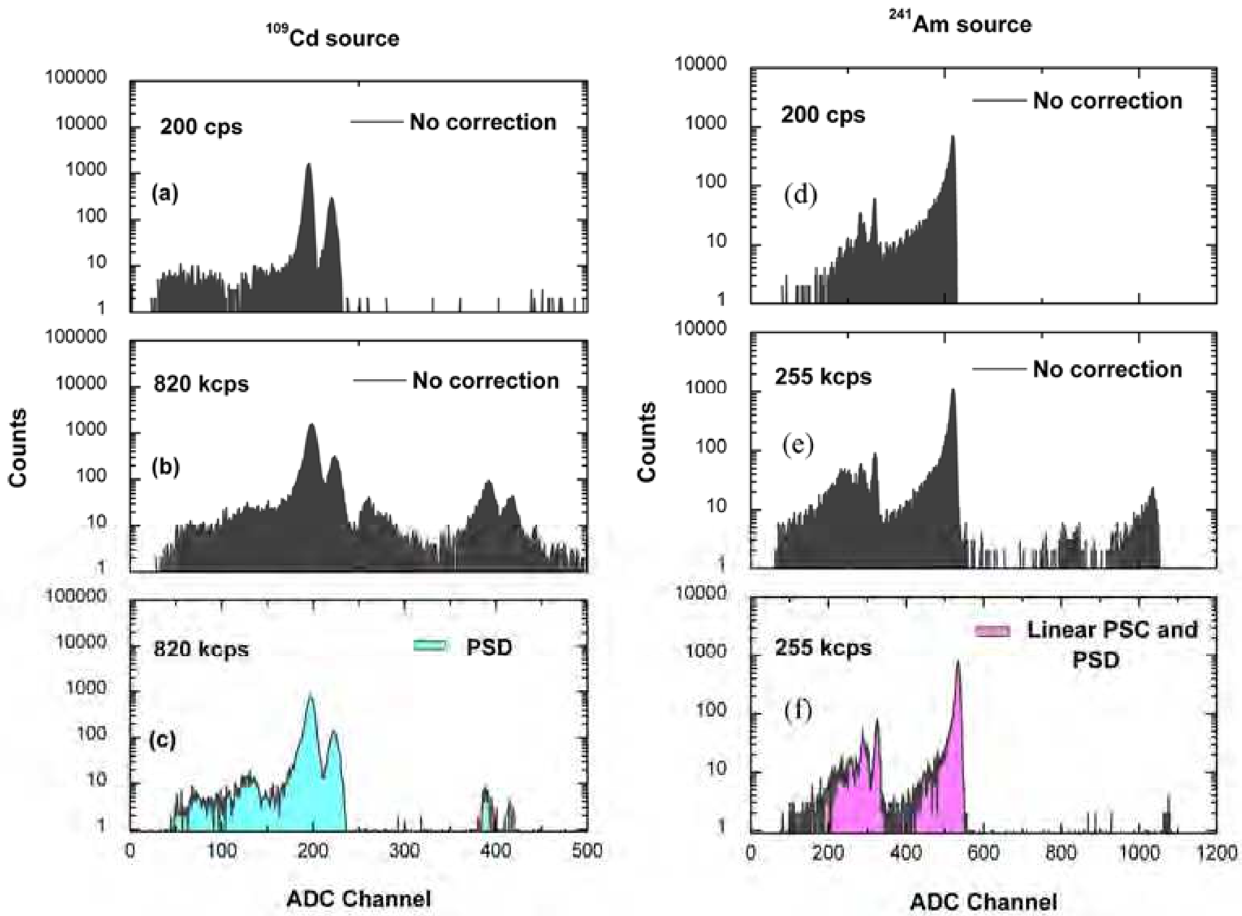

Fig. 12. Measured ^{109}Cd spectra at (a) 200 cps with no correction, (b) at 820 kcps with no correction and (c) at 820 kcps after PSD. Measured ^{241}Am spectra at (d) 200 cps with no correction, (e) at 255 kcps with no correction and (f) at 255 kcps after linear PSC.

We also measured X-ray spectra from a non clinical X-ray tube with different anode materials (Ag, Mo). In Figure 13 are shown the measured Ag-target X-ray spectra (32 kV) at 8.8 kcps with no correction, at 258 kcps with no correction and at 258 kcps after PSD. At high photon counting rate, the measured Ag spectrum, despite the good energy resolution of the peaks (22.1 and 24.9 keV), is characterized by a high background beyond the end point energy, due to the peak pile-up; while, after PSD, this background is quite similar to the spectrum at low photon counting rate. These results open up the possibility of precise estimations of the end point energy, i.e. the peak voltage of a X-ray tube, even at high photon counting rates. As well known, precise peak voltage measurements are essential for accurate quality controls on clinical X-ray tubes. Figures 13(d), (e) and (f) also show the measured Mo X-ray spectra.

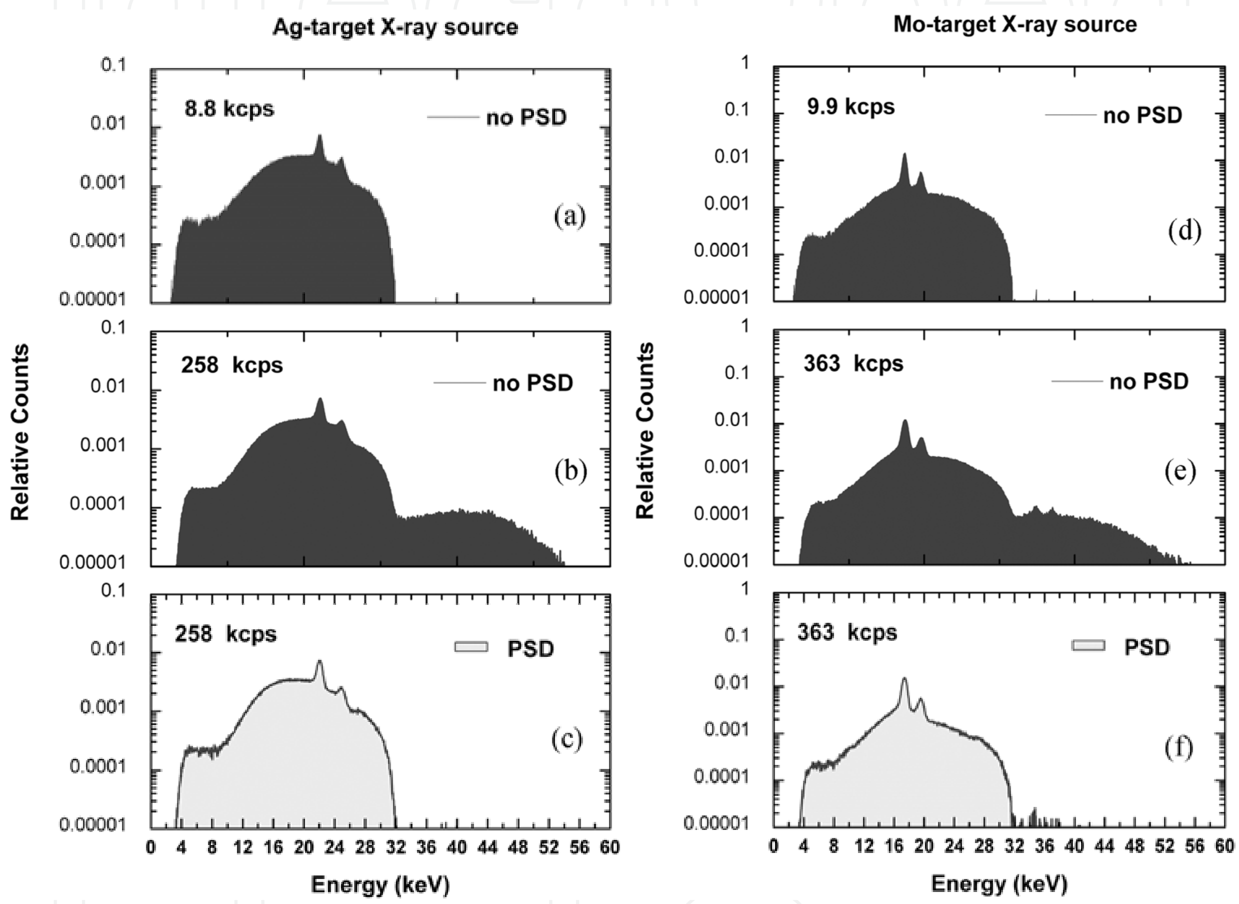

Fig. 13. Ag-target X-ray spectra (32 kV) at (a) 8.8 kcps with no correction, (b) at 258 kcps with no correction and (c) at 258 kcps after PSD. Mo-target X-ray spectra (32 kV) at (d) 9.9 kcps with no correction, (e) at 363 kcps with no correction and (f) at 363 kcps after PSD.

6. Direct measurement of mammographic X-ray spectra with the digital CdTe spectrometer: A medical application

Knowledge of energy spectra from X-ray tubes is a key tool for quality controls (QCs) in mammography. As well known, X-ray spectra directly influence the dose delivered to the patients as well as the image quality. X-ray spectra can be used for accurate estimations of the peak voltage (KVp) of the tubes, the energy fluence rate, the inherent filtration, the beam-hardening artifacts and for the correct implementation of the new dual-energy techniques.

By way of example, the peak voltage of a diagnostic X-ray tube should be routinely monitored, since small KVp changes can modify both absorbed dose and image contrast in mammography. With regard to dosimetric investigations, X-ray spectra can be also used to estimate the exposure, the air kerma and the absorbed energy distribution inside a breast tissue or a test phantom, overcoming the well known problem of the energy dependence of the response of the dosimeters (solid state detectors and ionization chambers) which are commonly used for the measurements of the absorbed energy distribution. Dosimeter calibrations, which usually involve complicated and time-consuming procedures, are a critical issue for routine investigations.

The spectrum emitted by a mammographic X-ray tube is, typically, obtained by analytical procedures based on semi-empirical models and Monte Carlo methods. In routine quality controls, insufficient information about some characteristic parameters of the X-ray tubes, such as the anode angle, the filters and the exact value of the applied tube voltage, could compromise the precision and the accuracy of the spectra. Of course, measurement of X-ray spectra would be the best procedure for accurate quality controls in mammography. Currently, routine measurement of mammographic X-ray spectra is quite uncommon due to the complexity of the measurement procedure. The measurement of mammographic X-ray spectra is a difficult task because of limitations on measurement with high energy resolution at high photon counting rates as well as geometrical restrictions, especially in a hospital environment.

In this section, we report on direct measurements of clinical molybdenum X-ray spectra by using the digital CdTe detection system.

6.1 Experimental set-up

Mo-target X-ray spectrum measurements were performed under clinical conditions (Istituto di Radiologia, Policlinico, Palermo). We used a Sylvia mammographic unit (Gilardoni) with a Mo anode tube (MCS, 50MOH), characterized by an additional filtration of 0.03 mm Mo and a 10° anode angle. The compression paddle was removed during the measurements. The detector was placed on the cassette holder with a 59.5 cm focal spot-detector distance. To reduce the photon counting rate on the detection system to an acceptable level, we used a pinhole collimator: a tungsten collimator disk, 1 mm thick with a 100 μm diameter circular hole, placed in front of the detector (over the beryllium window). Using this collimation setup, we measured X-ray spectra with a photon counting rate up to 453 kcps. It is well known that the choice of the proper collimation system is a critical issue for accurate measurements of X-ray spectra. An excessive reduction of the aperture and the thickness of the collimator can produce several distortions in the measured spectra (peaks and continuum events). These distortions are mainly due to (i) the penetration of photons through the collimator material, (ii) scattered photons from the collimator edges and (iii) characteristic X rays from the collimator material. The first effect can be reduced by choosing a proper collimator material and thickness. In the investigated energy range (1-30 keV), the penetration of photons through the 1 mm thick tungsten collimator is negligible, as demonstrated by the estimated values of the transmission equivalent aperture (*TEA*). By using the tabulated tungsten mass attenuation coefficient values (Boone & Chavez, 1996), we obtained a *TEA* equals to the collimator aperture area, showing that no photon penetration occurs. The other collimation distortions mainly depend on the alignment of the collimator with the X-ray beam and on the energy of the X-ray beam. Misalignment between the X-ray beam and the collimator can produce scattered photons and characteristic X rays from the collimator edge. Obviously, accurate alignment becomes more difficult as the thickness of the collimator increases and its aperture diameter decreases. The optimum collimation set-up should be a trade-off between the reduction of collimation distortions and the photon counting rate. To optimize the beam-detector alignment, the detector was mounted on an aluminum plate equipped with three micrometric screws. A preliminary focal spot-detector alignment was carried out with a laser pointer taking into account the reference marks positioned on both sides of the tube head, while a more accurate alignment was obtained by changing the plate orientation looking for the maximum photon counting rate and the absence of distortions in the measured spectra.

We also performed the measurement of attenuation curves through the measured Mo spectra. This curve, which is usually measured to characterize the spectral properties of a beam, was compared with that measured by using a standard mammographic ionization chamber (Magna 1cc together with Solidose 400, RTI Electronics) and a solid state dosimeter (R100, RTI Electronics). Exposure values from spectral data were obtained through the estimation of the energy fluence and the air mass energy absorption coefficients, as described in our previous work (Abbene et al., 2007). To measure the attenuation curves, we used a standard aluminum filter set (type 1100, Al 99,0 % purity, RTI electronics). To minimize the effects of scattered radiation, we performed the measurements in a "good geometry" condition, as suggested by several authors (Johns & Cunninghan, 1983); in particular, the experimental set-up for these measurements was characterized by a filter-detector distance of 42 cm.

6.2 Clinical X-ray spectra measurements

Figure 14(a) shows the measured Mo-target X-ray spectra under clinical conditions. The tube settings were: tube voltages of 26, 28 and 30 kV and tube current-time product of 20 mAs. The photon counting rates are 278, 362 and 453 kcps at 26, 28 and 30 kV, respectively.

Figure 14(b) shows the attenuation curves (28 kV and 20 mAs) obtained from the spectra measured with the digital system, from simulated spectra (IPEM Report 78) and by using the exposure values directly measured with the ionization chamber (Magna 1cc together with Solidose 400, RTI Electronics) and with the solid state dosimeter (R100, RTI Electronics). It is evident the good agreement among the curves obtained from the detector, the simulation and the ionization chamber. The disagreement with the attenuation curve obtained from the solid state dosimeter, points out the energy dependence of the dosimeter response. Since aluminum filters harden the X-ray beam and alter the energy spectrum, if dosimeter does not has a *flat* response for different spectra, the attenuation curve will be in error. The correction of the energy dependence of the dosimeter response need accurate calibrations which involve complicated and time-consuming procedures, critical for routine investigations.

These comparisons highlight two main aspects: (i) the ability of the digital system to perform accurate mammographic X-ray spectra without excessive time-consuming procedures and (ii) the possible use of this system both as dosimeter and for calibrations of dosimeters.

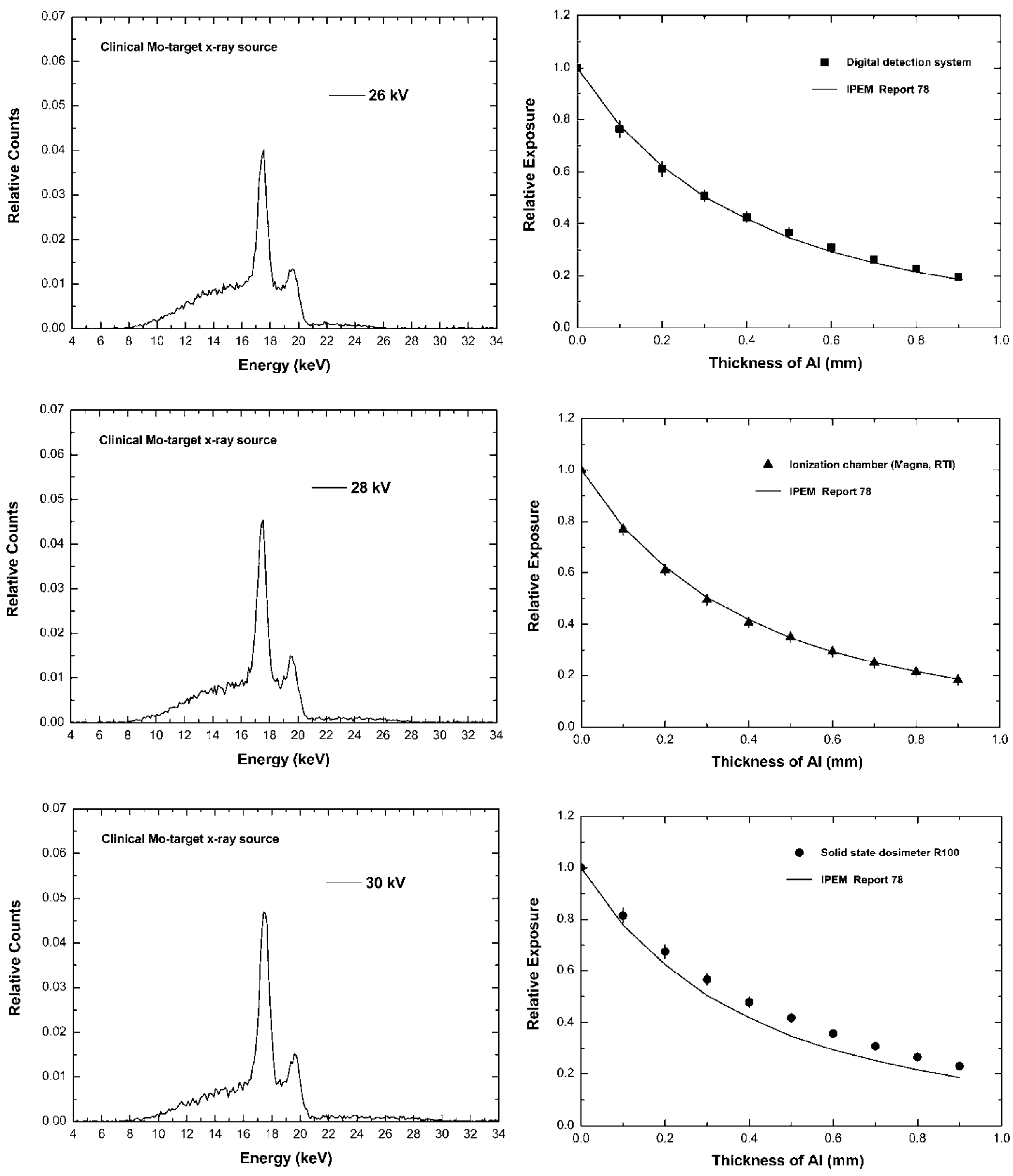

(a) (b)

Fig. 14. (a) Mo-target X-ray spectra (26, 28 and 30 kV; 20 mAs) measured with the digital system under clinical conditions; the counts were normalized to the total number of detected events. (b) Attenuation curves obtained from measured and simulated spectra and from direct exposure measurements (ionization chamber and solid state detector). The tube settings were: 28 kV and 20 mAs.

7. Conclusion

High-Z and wide band gap compound semiconductors are very promising materials for the development of portable high resolution spectrometers in the hard X-ray energy band (>15 keV). In particular, CdTe and CdZnTe detectors, due to the high atomic number, the high density and the wide band gap, ensure high detection efficiency, good room temperature performance and are very attractive for several X-ray applications. CdTe/CdZnTe detectors coupled to digital readout electronics show excellent performance and are very appealing for high-rate X-ray spectroscopy. The digital pulse processing (DPP) approach is a powerful tool for compensation of the effects of incomplete charge collection (typical of CdTe and CdZnTe detectors) and the effects due to high-rate conditions (baseline fluctuations, pile-up).

The performance of the presented prototype, based on a CdTe detector and on a custom DPP system, highlight the high potentialities of these systems especially at critical conditions. The digital system, combining fast and slow shaping, automatic pole-zero adjustment, baseline restoration, pile-up rejection and some pulse shape analysis techniques (pulse shape discrimination, linear and non linear corrections), is able to perform a correct estimation of the true rate of the impinging photons, a precise pulse height measurement and the reduction of the spectral distortions due to pile-up and incomplete charge collection. High-rate measurements (up to 800 kcps) highlight the excellent performance of the digital system: (i) low photopeak centroid shift, (ii) low worsening of energy resolution and (iii) the minimization of peak pile-up effects.

Measurements of clinical X-ray spectra also show the high potentialities of these systems for both calibration of dosimeters and advanced quality controls in mammography.

The results open up the development of new detection systems for spectral X-ray imaging in mammography, based on CdTe/CdZnTe pixel detectors coupled with a DPP system. Recently, single photon counting detectors are very appealing for digital mammography allowing the implementation of dual-energy techniques and improvements on the quality of images. In this contest, CdTe/CdZnTe pixel detectors can ensure better performance (energy resolution <5% at 30 keV) than the current prototypes based on silicon detectors (energy resolution of about 15% at 30 keV).

Future works will regard the development of a *real time* system, based on the digital method, by using a field programmable gate array (FPGA)technology.

8. References

Abbene, L. et al. (2007). X-ray spectroscopy and dosimetry with a portable CdTe device. *Nucl. Instr. and Meth. A,* Vol. 571, No. 1, (February 2007), pp. 373-377, ISSN 0168-9002

Abbene, L. et al. (2010). Performance of a digital CdTe X-ray spectrometer in low and high counting rate environment. *Nucl. Instr. and Meth. A,* Vol. 621, No. 1, (September 2010), pp. 447-452, ISSN 0168-9002

Abbene, L. et al. (2010). High-rate x-ray spectroscopy in mammography with a CdTe detector: A digital pulse processing approach. *Med. Phys.,* Vol. 37, No. 12, (December 2010), pp. 6147-6156, ISSN 0094-2405

Abbene, L., Gerardi, G. (2011). Performance enhancements of compound semiconductor radiation detectors using digital pulse processing techniques. *Nucl. Instr. and Meth. A,* in press, ISSN 0168-9002

Boone, J. M, Chavez, A. E. (1996). Comparison of x-ray cross sections for diagnostic and therapeutic medical physics. *Med. Phys.,* Vol. 23, No. 12, (December 1996), pp. 1997-2005, ISSN 0094-2405

Cavalleri, G. et al. (1971). Extension of Ramo theorem as applied to induced charge in semiconductor detectors. *Nucl. Instr. and Meth.,* Vol. 92, pp. 137-140, ISSN 0168-9002

Del Sordo, S. et al. (2004). Spectroscopic performances of 16 x 16 pixel CZT imaging hard-X-ray detectors. *Nuovo Cimento B.,* Vol. 119, No. 3, (March 2004) pp. 257-270, ISSN 1594-9982

Del Sordo, S. et al. (2009). Progress in the Development of CdTe and CdZnTe Semiconductor Radiation Detectors for Astrophysical and Medical Applications. *Sensors,* Vol. 9, No. 5, (May 2009), pp. 3491-3526, ISSN 1424-8220

Gerardi, G. et al. (2007). Digital filtering and analysis for a semiconductor X-ray detector data acquisition. *Nucl. Instr. and Meth. A,* Vol. 571, No. 1, (February 2007), pp. 378-380, ISSN 0168-9002

Hecht, K. (1932). Zum Mechanismus des lichtelektrischen Primärstromes in isolierenden Kristallen. *Z. Phys.,* Vol. 77, pp. 235-245

IEEE Standard (2003), ANSI N42.31, pp. 1-33

Jones, L. T., Woollam, P. M. (1975). Resolution improvement in CdTe gamma detectors using pulse-shape discrimination. *Nucl. Instr. and Meth.,* Vol. 124, No. 2, (March 1975), pp. 591-595, ISSN 0168-9002

Johns, H. E., Cunninghan, J. R. (1983). *The Physics of Radiology* (4th Ed.), C. C. Thomas Publisher, ISBN 0-398-04669-7, Springfield

Keele, B. D. et al. (1996). A method to improve spectral resolution in planar semiconductor gamma-ray detectors. *IEEE Trans. Nucl. Sci.,* Vol. 43, No. 3, (June 1996), pp. 1365-1368, ISSN 0018-9499

Knoll, G. F. (2000). *Radiation Detection and Measurement* (3rd Ed.), Wiley, ISBN 978-047-1073-38-3, New York

McGregor, D. S., Hermon, H. (1997). Room-temperature compound semiconductor radiation detectors. *Nucl. Instr. and Meth. A,* Vol. 395, No. 1, (August 1997), pp. 101-124, ISSN 0168-9002

Owens, A., Peacock, A. (2004). Compound semiconductor radiation detectors. *Nucl. Instr. and Meth. A,* Vol. 531, No. 1, (September 2004), pp. 18-37, ISSN 0168-9002

Ramo, S. (1939). Currents induced by electron motion. *Proceedings of the I.R.E.,* pp. 584-585

Shockley, W. (1938). Currents to conductors induced by a moving point charge. *J. Appl. Phys,* Vol. 9, pp. 635-636, ISSN 0021-8979

Sjöland, K. A., Kristiansson, P. (1994). Pile-up and defective pulse rejection by pulse shape discrimination in surface barrier detectors. *Nucl. Instr. and Meth. B,* Vol. 94, No. 3, (November 1994), pp. 333-337, ISSN 0168-583X

Takahashi, T., Watanabe, S. (2001). Recent progress in CdTe and CdZnTe detectors. *IEEE Trans. Nucl. Sci.,* Vol. 48, No. 4, (August 2001), pp. 950-959, ISSN 0018-9499

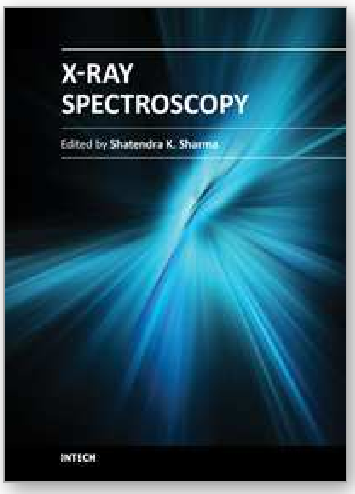

X-Ray Spectroscopy
Edited by Dr. Shatendra K Sharma

ISBN 978-953-307-967-7
Hard cover, 280 pages
Publisher InTech
Published online 01, February, 2012
Published in print edition February, 2012

The x-ray is the only invention that became a regular diagnostic tool in hospitals within a week of its first observation by Roentgen in 1895. Even today, x-rays are a great characterization tool at the hands of scientists working in almost every field, such as medicine, physics, material science, space science, chemistry, archeology, and metallurgy. With vast existing applications of x-rays, it is even more surprising that every day people are finding new applications of x-rays or refining the existing techniques. This book consists of selected chapters on the recent applications of x-ray spectroscopy that are of great interest to the scientists and engineers working in the fields of material science, physics, chemistry, astrophysics, astrochemistry, instrumentation, and techniques of x-ray based characterization. The chapters have been grouped into two major sections based upon the techniques and applications. The book covers some basic principles of satellite x-rays as characterization tools for chemical properties and the physics of detectors and x-ray spectrometer. The techniques like EDXRF, WDXRF, EPMA, satellites, micro-beam analysis, particle induced XRF, and matrix effects are discussed. The characterization of thin films and ceramic materials using x-rays is also covered.

InTech Europe
University Campus STeP Ri
Slavka Krautzeka 83/A
51000 Rijeka, Croatia
Phone: +385 (51) 770 447
Fax: +385 (51) 686 166
www.intechopen.com

InTech China
Unit 405, Office Block, Hotel Equatorial Shanghai
No.65, Yan An Road (West), Shanghai, 200040, China
中国上海市延安西路65号上海国际贵都大饭店办公楼405单元
Phone: +86-21-62489820
Fax: +86-21-62489821